CHEMISTRY
A EUROPEAN JOURNAL

ChemPubSoc Europe

DOI: 10.1002/chem.201200255

Ionic-Liquid-Mediated Active-Site Control of MoS_2 for the Electrocatalytic Hydrogen Evolution Reaction

Vincent Wing-hei Lau,[a] Anthony F. Masters,[a] Alan M. Bond,[b] and Thomas Maschmeyer*[a]

Abstract: The layered crystal MoS_2 has been proposed as an alternative to noble metals as the electrocatalyst for the hydrogen evolution reaction (HER). However, the activity of this catalyst is limited by the number of available edge sites. It was previously shown that, by using an imidazolium ionic liquid as synthesis medium, nanometre-size crystal layers of MoS_2 can be prepared which exhibit a very high number of active edge sites as well as a de-layered morphology, both of which contribute to HER electrocatalytic activity. Herein, it is examined how to control these features synthetically by using a range of ionic liquids as synthesis media. Non-coordinating ILs with a planar heterocyclic cation produced MoS_2 with the de-layered morphology, which was subsequently shown to be highly advantageous for HER electrocatalytic activity. The results furthermore suggest that the crystallinity, and in turn the catalytic activity, of the MoS_2 layers can be improved by employing an IL with specific solvation properties. These results provide the basis for a synthetic strategy for increasing the HER electrocatalytic activity of MoS_2 by tuning its crystal properties, and thus improving its potential for use in hydrogen production technologies.

Keywords: electrochemistry · heterogeneous catalysis · hydrogen · ionic liquids · molybdenum sulfide

Introduction

Hydrogen will become an increasingly important commodity in the future, since it has been proposed as the principal energy carrier in the hydrogen-economy paradigm.[1] Presently, the dominant method for hydrogen production is alkane reforming, a process that usually depends on non-renewable fossil-based feedstocks and releases CO and CO_2 as environmentally harmful by-products. Furthermore, the presence of CO is undesirable even in trace amounts, as it can poison the noble metal electrocatalysts in a hydrogen fuel cell. Hydrogen production by the electrochemical splitting of water, therefore, offers a cleaner alternative (provided that a renewable source of electricity is used), as this process yields only hydrogen and oxygen as products, and because the availability of the precursor, water, is essentially limitless. However, for this reaction to proceed at a satisfactory rate, expensive electrocatalysts are often required. For example, the best electrocatalysts for one of the half-reactions of water splitting, the hydrogen evolution reaction (HER, $2H^+ + 2e^- \rightarrow H_2$), are platinum and the other noble metals.[2] Hence, for the water-splitting reaction to be an economical process of hydrogen production, the electrocatalyst needs to be sufficiently active while either minimising the use of noble metals, or employing non-precious alternatives. Furthermore, intricate coordination or organometallic catalysts should be avoided, as the increased complexity of the overall catalyst system will lead to a higher cost of catalyst preparation. Thus, hydrogen-evolving catalysts such as hydrogenase[3] and nitrogenase[4] are unsuitable for large-scale applications, despite the fact that they are highly active and employ inexpensive metals.

The HER electrocatalyst system investigated here is the layered crystal MoS_2, the edges of which bear a close resemblance both structurally and electronically to the edges of the active centre of the nitrogenase enzyme.[5] The activity of MoS_2 for HER has indeed been experimentally verified: MoS_2 has an activity of $1.64\times10^{-2}\ s^{-1}$ based on turnover per active site.[6] Since the HER activity of MoS_2 is only 57 times lower than that of platinum ($9.4\times10^{-1}\ s^{-1}$ for the Pt-(111) surface plane), whilst being more than 1000 times cheaper (based on the price of the molybdenum and platinum), MoS_2 has been proposed as an inexpensive candidate catalyst for HER. However, the activity of MoS_2 is limited by the population of its active edges, which only constitute a small proportion of the total surface area. The majority of the molybdenum and sulfur atoms occupy the interior of the crystal layer to form the basal planes, which account for the majority of total surface area but are catalytically inactive. To explore the potential of MoS_2 as a practical HER electrocatalytic alternative to the noble metals, it is necessary to improve its activity by maximising the number of active edge sites.

[a] Dr. V. W.-h. Lau, Prof. A. F. Masters, Prof. T. Maschmeyer
Laboratory of Advanced Catalysis for Sustainability
School of Chemistry,
University of Sydney, NSW, 2006 (Australia)
Fax: (+61) 2-9351-3329
E-mail: th.maschmeyer@chem.usyd.edu.au

[b] Prof. A. M. Bond
School of Chemistry, Monash University
Clayton, Victoria, 3800 (Australia)

One route to increasing the number of active edges is to decrease the size of the MoS_2 layers to nanometre dimensions. We previously reported such a synthetic route whereby MoS_2 crystals were prepared by thermal decomposition of $(NH_4)_2MoS_4$ in 1-alkyl-3-methylimidazolium triflate ionic liquids (ILs) $[C_1C_nIM][OTf]$.[7] The choice of an IL as solvent was based on the observation that active surfaces in crystalline catalysts are usually under-coordinated high-energy surfaces,[8] and that ILs have been reported to stabilise highly energetic, thermodynamically unstable surface features in crystals.[9] In this study, the IL-synthesised MoS_2 samples not only displayed greater electrocatalytic activity for HER than the control samples, but also exhibited several important morphological changes. Specifically, the IL-synthesised samples consisted of smaller and more unstacked MoS_2 layers compared to the controls. The origin of this unstacked/de-layered morphology demands further investigation, as it may impact on the catalytic activity in several ways. Firstly, TEM analysis suggests that such morphology increases the exposure of the MoS_2 layer edges, and may improve diffusion of substrate and product to and from the reaction centres. Secondly, this de-layered morphology is known to affect the relative rates of hydrodesulfurisation and hydrogenation in aromatic sulfur-containing compounds.[10] This morphology–selectivity relationship is rationalised by the rim-edge model,[10a] which proposed that hydrogenation occurs exclusively on the rim sites, that is, the edges on the top and bottom layers of the MoS_2 stacks, whereas sulfur hydrogenolysis is proposed to occur on both the rim and edge sites, the latter of which are all of the edge sites on the layers between the top and bottom of the stacks. One hydrodesulfurisation/hydrogenation study has suggested that the inflection points at the curvature of unsupported MoS_2 layers may also act as the hydrogenation active site, and that the number of these points increases as the MoS_2 layers become more unstacked.[11] Given the number of potential effects this de-layered morphology has on the catalytic properties of MoS_2, it is of fundamental and practical interests to systematically elucidate this morphology–activity relationship for HER electrocatalysis. Thus, the objectives of the present study were to develop a method of synthetically controlling this de-layered morphology and investigate the aforementioned morphology–activity relationship, with the ultimate goal of exploiting any benefit to the catalyst activity arising from unstacking of the MoS_2 layers.

One potential cause of de-layering in the IL-synthesised MoS_2 is that the aromaticity of the imidazolium IL disrupts the van der Waals interactions holding the MoS_2 layers together. Several literature examples support this "de-layering-via-aromaticity" hypothesis and it is one that will be examined closely in this study.[12] For example, imidazolium ILs have been reported to untangle bundles of carbon nanotubes[12b,c] and exfoliate graphite into graphene;[12d] these phenomena were attributed to disruption of the graphitic π–π interactions by the aromatic cation. Moreover, adsorption of conjugated and aromatic compounds onto the basal planes of the MoS_2 layers has been shown to be energetically favourable.[12a,e] To test whether unstacking/de-layering is caused by the aromaticity of the IL, three aromatic and three non-aromatic ILs (Figure 1) were employed as solvent for the synthesis of MoS_2. As several of these ILs lack physicochemical data in the literature, they were thoroughly characterised by NMR, ESI-MS and, in particular, thermogravimetric analysis (TGA) to ensure that they have the required thermal stability for the synthesis. The six ILs were used to prepare six samples of MoS_2 by thermal decomposition of $(NH_4)_2MoS_4$ following a modified version of the protocol described previously.[7] The six samples are denoted by the solvent employed in the synthesis. These MoS_2 samples were characterised morphologically and evaluated for their HER electrocatalytic performance, with particular focus on how the differing morphologies affected their catalytic activity.

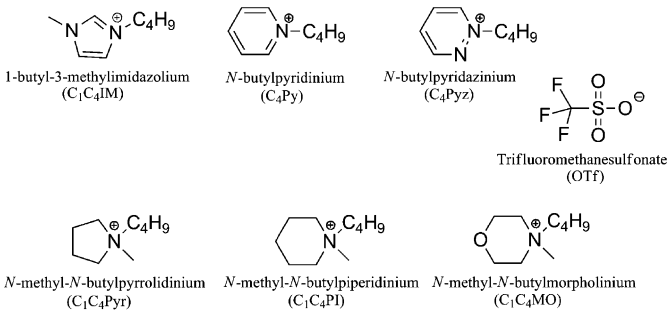

Figure 1. Structures and notations of the three aromatic and the three non-aromatic ILs. The counterion common to all ILs is the trifluoromethanesulfonate anion.

Results and Discussion

Characterisation: The procedure for the synthesis of MoS_2 involved a more rigorous purification step than that reported previously.[7] Specifically, the black MoS_2 powder samples were washed with ethanol, water, acetone and hexane (as opposed to only with ethanol) to ensure complete removal of the reactants and the IL. The absence of strong aliphatic CH stretching bands in the FTIR spectra (Figure 2) in the region between 3000 and 2000 cm^{-1} for all six samples is consistent with removal of the IL from the MoS_2 powder. Other IR features are observed in the region between 2000 and 1000 cm^{-1}, specifically a broad band at 1600 cm^{-1}, corresponding to adsorbed water on air-contacted MoS_2,[13] and bands centred around 1500 and 1300 cm^{-1}, which correspond to removable surface-bound ammonia from decomposition of $(NH_4)_2MoS_4$.[14] Moreover, as the MoS_2 samples were stored in air, bands attributable to surface oxide species were evident in the region of 1100–1000 cm^{-1}.[13] This molybdenum oxide species on the surface is the predominant feature in all six samples, as observed in their Raman spectra at 514 nm excitation (Figure 3), where the phonons corresponding to MoO_3[15] are more intense than those of MoS_2.[16] This observation indicates that the surface is principally composed of the oxide, likely due to the large amount

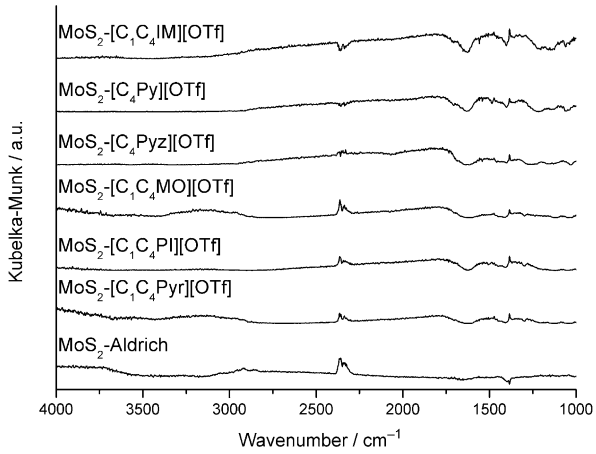

Figure 2. FTIR spectra of the MoS_2 samples; the sharp signals at $\approx 2400\ cm^{-1}$ correspond to atmospheric carbon dioxide, while the broad signal centred at $\approx 3200\ cm^{-1}$ corresponds to moisture from the atmosphere or from the KBr matrix. The spectrum of a commercial sample of MoS_2 from Aldrich is shown for comparison.

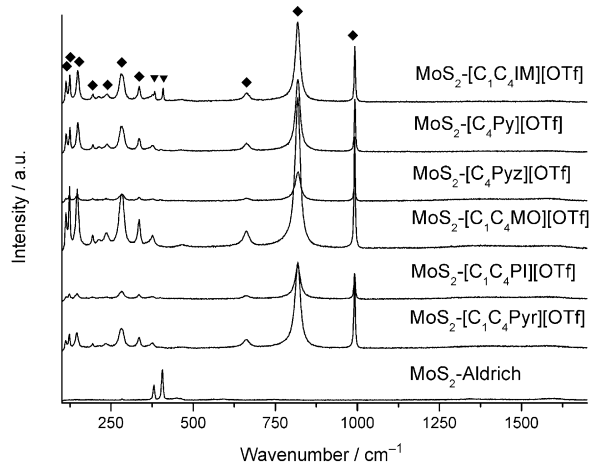

Figure 3. Raman spectra of the MoS_2 samples at 514 nm excitation (▼: MoS_2 phonons; ◆: MoO_3 phonons). The spectrum of a commercial sample of MoS_2 from Aldrich is shown for comparison.

of reactive surfaces susceptible to atmospheric oxidation. The bulk of the samples, however, is definitively composed of MoS_2 rather than MoO_3, given the absence of the MoO_3 reflections in their XRD patterns, as shown in Figure 4.

The two key features in the XRD patterns are the reflections corresponding to single-layer MoS_2 sheets (i.e., intra-layer ordering)[17] and the absence of the (002) reflection, the latter corresponding to the 6 Å inter-layer spacing of stacked MoS_2. Amongst the IL-synthesised MoS_2 samples, MoS_2-[C_1C_4IM][OTf] and MoS_2-[C_4Py][OTf] have higher crystallinity than the others, as evident from their sharper (100) and (110) intra-layer reflections. The higher crystallinity of these samples is an important factor when evaluating their electrocatalytic activity for HER, since crystallinity affects the formation of well-defined active edge sites.[18] The absence of the (002) reflection in all six IL-synthesised samples suggests that the MoS_2 layers do not stack to a significant height, and that stacks do not appear frequently in the sample. The nanometre-scale arrangement of the MoS_2 layers and bulk morphology of these six samples were analysed by TEM and SEM (Figures 5 and 6, respectively).

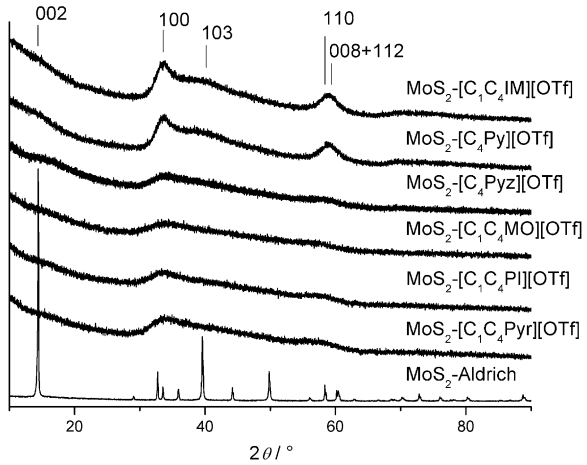

Figure 4. XRD patterns of the six MoS_2 samples, indexed to single-layer 2H-MoS_2.[17] The pattern of a commercial sample of MoS_2 from Aldrich is shown for comparison.

With the exception of MoS_2-[C_4Pyz][OTf], SEM analysis shows that all of the MoS_2 samples have a spherical morphology with diameters of 200–300 nm, indicative of a radial growth mechanism from well-solubilised precursors.[19] The surfaces of these spherical particles consist of MoS_2 layers of differing degree of unstacking/de-layering, as observable under TEM analysis. This de-layered morphology is most pronounced in MoS_2-[C_4Py][OTf] and MoS_2-[C_1C_4IM][OTf], in which the MoS_2 layers are peeling away from the surface of the spherical particles. This morphology, however, is also observable in MoS_2-[C_1C_4Pyr][OTf], in contradiction to the de-layering-via-aromaticity hypothesis. The de-layered morphology is present to a much lesser extent in MoS_2-[C_1C_4MO][OTf] and MoS_2-[C_1C_4PI][OTf]. MoS_2-[C_4Pyz]-[OTf] appears to be an outlying result: SEM showed that the sample has both nanometre-sized spheres, indicative of radial crystallisation from solubilised precursor, and micrometer-sized prisms similar to bulk MoS_2. This bimodal morphology can be attributed to the presence of both solubilised and non-solubilised precursors, which leads to a bifurcation in morphological outcome. It is uncertain why this IL is less efficient in solubilising the thiomolybdate precursor than the other five ILs. However, this is the only IL in the set that has an electron lone pair, which can affect the intermolecular properties of this solvent. Furthermore, TEM analysis showed that neither of these two morphologies exhibited unstacking of the MoS_2 layers. One explanation is that the IL–MoS_2 interaction(s) required to unstack the layers were not present, but instead other interactions, especially coordination bonding, were more favourable and hence dominant. This explanation is supported by the fact that aromatic heterocycles containing multiple nitrogen atoms (e.g., pyrimidine and pyrazine) are known to form stable complexes with molybdenum over a number of oxidation states (4–

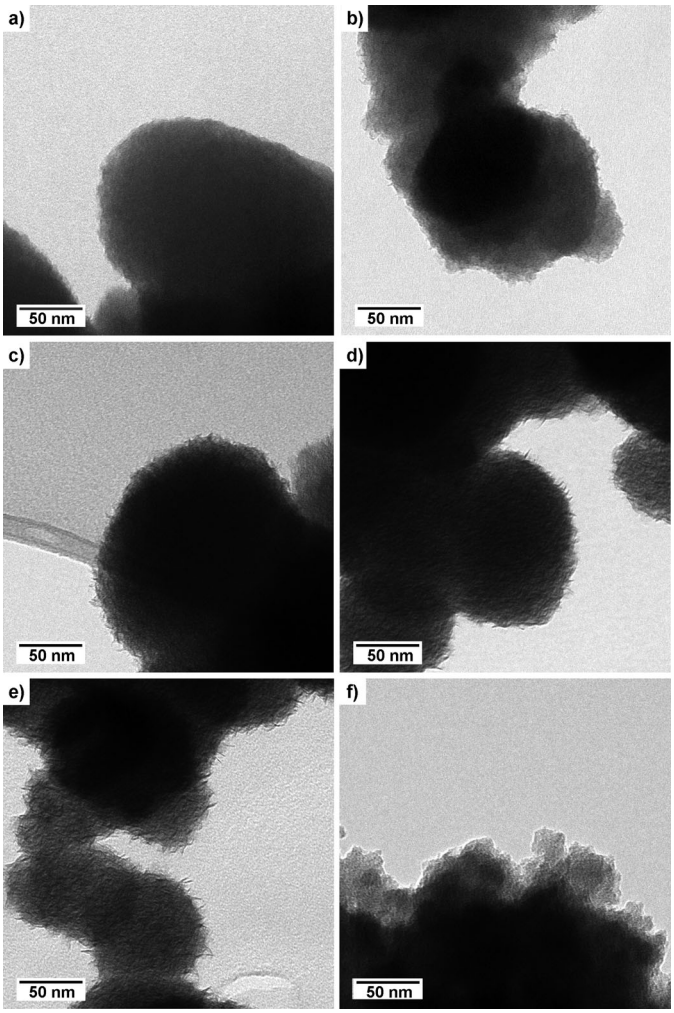

Figure 5. TEM at 10^5 magnification of MoS_2 synthesised in ILs. a) [C_1C_4PI][OTf]. b) [C_1C_4MO][OTf]. c) [C_1C_4Pyr][OTf]. d) [C_4Py][OTf]. e) [C_1C_4IM][OTf]. f) [C_4Pyz][OTf].

6),[20] that is, this IL may co-ordinate to both the thiomolybdate precursor and the MoS_2 product.

For the remaining five MoS_2 samples, the evidence here demonstrates that not only is the de-layered morphology observed when MoS_2 is synthesised in non-coordinating aromatic ILs in agreement with the hypothesis, but also that this morphology is observed when the aliphatic IL [C_1C_4Pyr][OTf] is employed. Presumably, heterocycles of fewer than five members are sufficiently planar to interact with the MoS_2 basal surfaces and prevent the layers from stacking together, while those with six or more members (morpholinium and piperidinium) are less efficient for this role, due to ring buckling in the boat/chair conformation. These results indicate that synthetic control over this unstacking/de-layering trend is achievable by employing ILs with the desired intermolecular interactions as synthesis media. This morphological control thus enables an investigation into the structure–functionality relationships between the different morphologies and the HER electrocatalytic activities of the various MoS_2 samples.

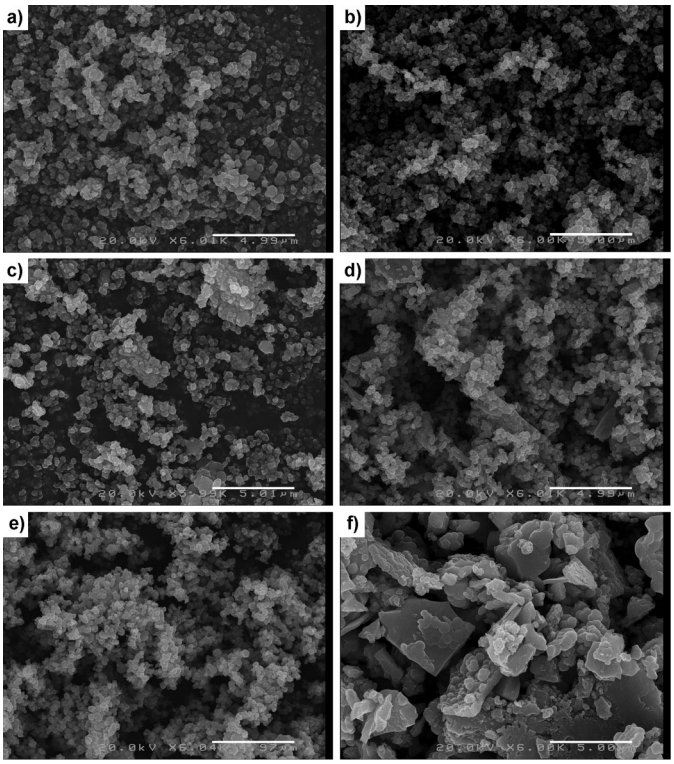

Figure 6. SEM at 6000 magnification of MoS_2 synthesised in ILs. a) [C_1C_4PI][OTf]. b) [C_1C_4MO][OTf]. c) [C_1C_4Pyr][OTf]. d) [C_4Py][OTf]. e) [C_1C_4IM][OTf]. f) [C_4Pyz][OTf]. The scale bar in each micrograph corresponds to 5 μm.

To meaningfully rank the electrocatalytic performance, the BET surface areas were characterised as well by nitrogen sorption (Table 1). It is evident that the de-layered morphologies correlate with the BET surface area: the three samples with the de-layered morphology—MoS_2-[C_4Py]-[OTf], MoS_2-[C_1C_4IM][OTf] and MoS_2-[C_1C_4Pyr][OTf]—all have surface areas in the hundreds of $m^2 g^{-1}$, whereas the samples without this morphology have values below $30\ m^2 g^{-1}$. The results are consistent with the fact that, when the MoS_2 layers are in an unstacked arrangement, there is greater exposure of the top and bottom basal surfaces of the MoS_2 layers that are accessible by the sorbent molecules.

Table 1. BET surface areas of the MoS_2 samples, calculated from the adsorption branch of the nitrogen sorption isotherm at 77 K. The surface area of a commercial sample of MoS_2 from Aldrich is shown for comparison.

		BET surface area [$m^2 g^{-1}$]
control	MoS_2-Aldrich	8.3
aromatic	MoS_2-[C_1C_4IM][OTf]	203
	MoS_2-[C_4Py][OTf]	147
	MoS_2-[C_4Pyz][OTf]	15.3
non-aromatic	MoS_2-[C_1C_4MO][OTf]	18.7
	MoS_2-[C_1C_4PI][OTf]	29.1
	MoS_2-[C_1C_4Pyr][OTf]	201

HER electrocatalysis: HER electrocatalytic activities of the six MoS_2 samples were evaluated with a rotating electrode under acidic conditions by two methods: 1) the standard Levich–Koutecky experimental protocols for the determination of the limiting current I_K; and 2) time-based single-potential coulometry for estimating the turnover frequency (TOF), assuming a 100% Faradaic efficiency for HER and that all 10 μg of MoS_2 powder on the electrode participated in the electrocatalytic reduction. Polarisation curves and the corresponding Tafel plots are shown in Figure 7, Levich–Koutecky plots in Figure 8 and time–current plots in Figure 9. I_K, Tafel slopes and TOFs for the six IL-synthesised MoS_2 samples, together with those of the two controls—MoS_2-[Aldrich] and the unmodified glassy carbon electrode (GCE)—are summarised in Table 2.

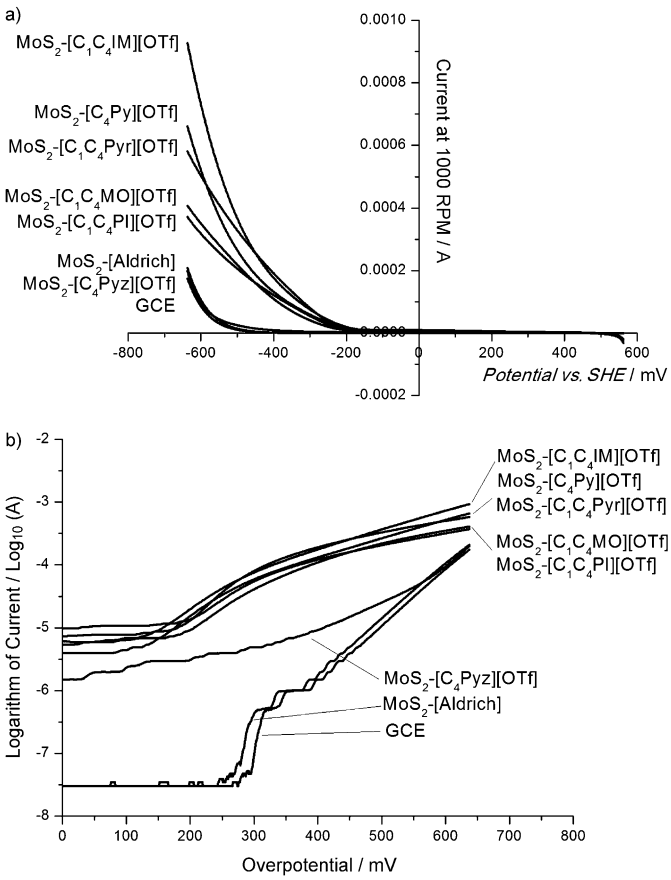

Figure 7. a) Linear-scan voltammogram at 1000 rpm and b) the corresponding Tafel plot.

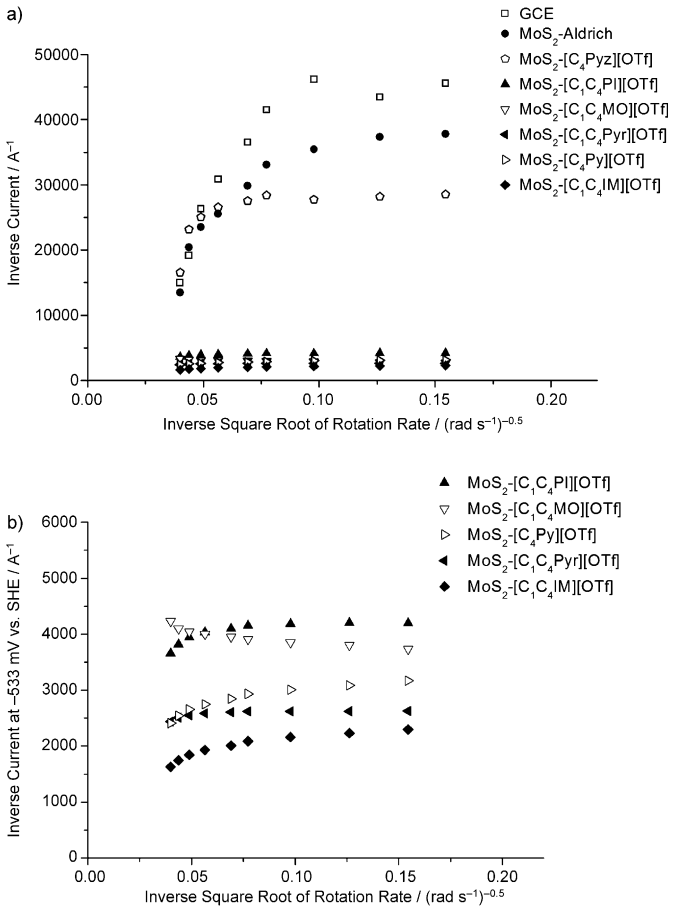

Figure 8. a) Levich–Koutecky plot of the HER current at −533 mV and b) the same plot reproduced in the inverse-current range of 0–6000 A^{-1}. As turbulent flow or edge effects manifest at rotation rates above 1600 rpm (below an inverse square root of rotation rate of 0.077), the limiting current I_K (y intercept) was determined by linear fitting of the data points at scan rates between 400 and 1600 rpm (inverse square root of rotation rate 0.77–0.16).

From the voltammetric curves, the onset potential of HER for all of the IL-synthesised MoS_2, with the exception of MoS_2-[C_4Pyz][OTf], is approximately −200 mV, a value consistent with nanometre-sized MoS_2 platelets.[6] Tafel plots of the IL-synthesised MoS_2 samples, not including MoS_2-[C_4Pyz][OTf], showed two regions with different gradients. The first region is below an overpotential of 300 mV, where

Table 2. Electrochemical data of the six IL-synthesised MoS_2 samples, compared to those of the two controls.

		I_K at −533 mV [μA]	Tafel slope below 300 mV overpotential [mV decade^{-1}]	Tafel slope above 300 mV overpotential [mV decade^{-1}]	TOF [10^3 s^{-1}]
control	GCE	30.8	–	111	3.9
	Aldrich	34.4	–	112	2.2
aromatic	C_1C_4IM	529	156	323	48
	C_4Py	370	154	334	32
	C_4Pyz	37.8	–	205	3.7
non-aromatic	C_1C_4Pyr	382	114	481	25
	C_1C_4PI	243	161	483	11
	C_1C_4MO	245	147	401	11

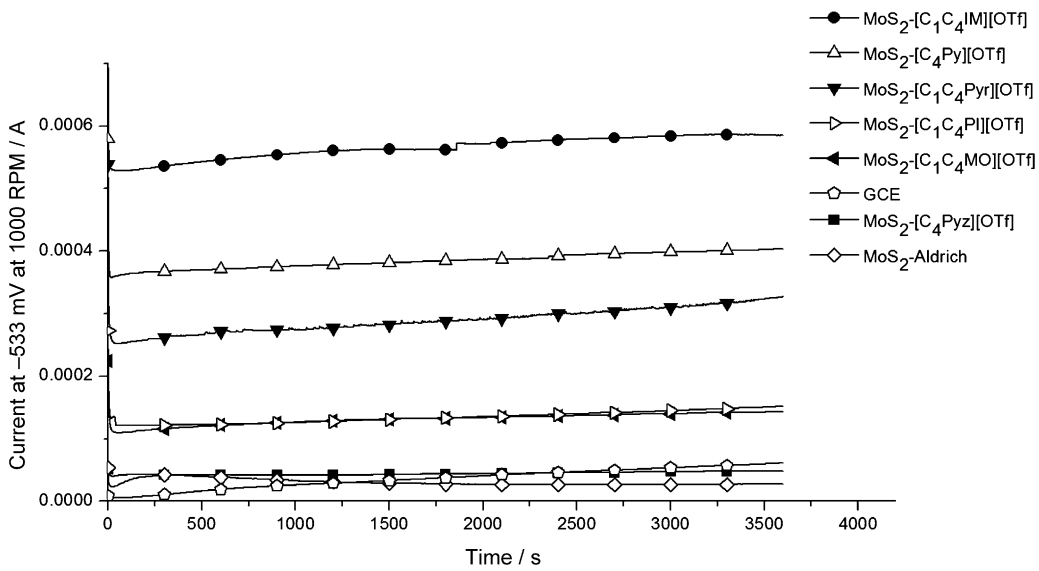

Figure 9. Single-potential time-based plot with the working electrode held at −533 mV at 1000 rpm. Each plot was integrated from the region where the current reached a plateau value to yield the number of charges passed. Turnover frequency was estimated by assuming a Faradaic efficiency of 100% and that all 10 μg of the MoS_2 powder deposited onto the electrode was involved in the electrocatalysed reaction.

the five samples yielded Tafel slopes between 114–161 mV decade^{-1}. Literature values for the Tafel slope are either 60 or 120 mV decade^{-1}, depending on the preparative method of MoS_2.[6] Nonetheless, the values obtained in this work are close to the theoretical slope of 120 mV decade^{-1} for HER electrocatalysts, in which adsorption of protons is the rate-limiting step.[21] This mechanism is consistent with the position of MoS_2 in the volcano plot where the Gibbs free energy of forming a surface catalyst–hydrogen bond is positive,[6b] that is, non-spontaneous hydrogen adsorption in which the surface coverage of the catalyst with hydrogen does not reach saturation. In the second region above an overpotential of 300 mV, the five samples yielded slopes in excess of 300 mV decade^{-1}. This is attributed to diffusion limitations of the substrate through the voids between the nanometre-sized particles. The outlying sample, MoS_2-[C_4Pyz][OTf], displayed essentially similar electrocatalytic properties to the two controls, MoS_2-[Aldrich] and the GCE, with an onset potential of around −400 mV. Its Tafel slope is twice that of the two controls, and may also be attributed to diffusion limitations, given that this sample has much finer particles than MoS_2-[Aldrich].

The order of activity of the MoS_2 samples, based on both I_K from the Levich–Koutecky plot and the TOF from coulometry, is MoS_2-[C_1C_4IM][OTf] > MoS_2-[C_4Py][OTf] ≈ MoS_2-[C_1C_4Pyr][OTf] > MoS_2-[C_4PI][OTf] ≈ MoS_2-[C_1C_4MO]-[OTf] > MoS_2-[C_4Pyz][OTf] ≈ MoS_2-[Aldrich] ≈ GCE. From the time–current plot, the electrocatalytic activity is sustained over a one-hour period for all MoS_2 samples; for some of the MoS_2 samples, this indicates that the electrocatalysts are active and stable for more than one hundred turnovers. The presence of the surface oxide, as observed in the Raman spectra above, is not expected to affect the electrocatalytic HER activity, because oxides of molybdenum, such as MoO_3, are not only inactive for HER,[22] but also electrochemically unstable and tend to be reduced under the acidic conditions and the potential applied in this work, in accordance with the Pourbaix diagram for molybdenum oxide.[23] While it is not certain whether the surface after electrochemical reduction is terminated by molybdenum (removal of surface oxygen atoms) or sulfur (removal of molybdate-like species), the steady currents observed in the single-potential time-based plot indicate that the resulting surface is catalytically active for HER.

The order of activity for the MoS_2 electrocatalysts showed a clear correlation between the morphology and the HER electrocatalytic performance of the MoS_2 samples. The three most active samples consisted of spherical particles with diameters of 100–300 nm and exhibited the unstacked/de-layered morphology. Both MoS_2-[C_1C_4PI][OTf] and MoS_2-[C_1C_4MO][OTf], which also consisted of spherical particles with similar diameters but without the de-layered morphology, exhibited lower activity. The least active electrocatalyst is MoS_2-[C_4Pyz][OTf], which has identical activity to MoS_2-[Aldrich]. This result is not unexpected since, from SEM analysis, MoS_2-[C_4Pyz][OTf] consisted of predominantly prism-shaped particles, which is the identical morphology to the commercial MoS_2 sample. Therefore, this result clearly demonstrates that the de-layered morphology is beneficial for HER electrocatalysis, due either to better exposure of the active edges and therefore improved substrate/product transfer to and from the active sites, or to the presence of additional active sites in the form of the inflection points at the curvature of the MoS_2 layers. The quantification of active sites in future experiments may elucidate which of the two is the major contributor to the increase in activity.

Furthermore, there are significant differences in electrocatalytic activity amongst the three MoS_2 samples with de-lay-

ered morphology. If one assumes that the extent of de-layering is correlated with the BET surface area (due to exposure of the basal planes), the results indicate that there is an additional factor that contributed to either the higher activity of MoS_2-[C_1C_4IM][OTf] over MoS_2-[C_1C_4Pyr][OTf], or the increase of activity of MoS_2-[C_4Py][OTf] to such an extent that it became comparable to that of MoS_2-[C_1C_4Pyr][OTf], despite having a significantly lower BET surface area. One distinguishing feature of MoS_2-[C_1C_4IM][OTf] and MoS_2-[C_4Py][OTf] is that their intralayer crystal reflections in their XRD patterns are more defined than those arising from the other four MoS_2 samples, that is, these two samples are more crystalline. Since crystallinity is desirable for the formation of well-defined active edge sites,[18] it is the factor to which the improved catalytic performance of these two samples is attributed. Given that the properties of the synthesis media are known to affect the crystal properties, it is noteworthy that both non-coordinating aromatic ILs yielded MoS_2 with better crystallinity than the non-aromatic ILs of similar molecular size. This effect may be rationalised by the examination of several literature postulates. For example, Wu et al. claimed that the crystallinity (in terms of crystal size and lattice strain) of TiO_2, and hence its photocatalytic activity, can be controlled by using solvents of different dielectric constants in a solvothermal synthetic route, with solvents of small dielectric constant yielding products of higher crystallinity.[24] They attributed this solvent effect to a reduction in precursor solubility as the dielectric constant of the solvent is reduced. This, they claimed, leads to a supersaturation of crystal nuclei and faster crystal growth and, through Ostwald ripening, yields product of larger crystal size and lower lattice strain. We also recently showed that the activity of the photocatalyst CdS is heavily dependent on the solvating ability of the synthesis medium, quantified by using the Reichardt solvatochromic betaine and E_T polarity scale.[25] Thus, the solvation properties of the ILs may explain the improved crystallinity of MoS_2-[C_1C_4IM][OTf] and MoS_2-[C_4Py][OTf]. As solvent parameters of trifluoromethanesulfonate ILs are scarce in the literature, the solvation parameters of the corresponding *N,N*-bis(trifluoromethanesulfonyl)imide (NTf_2) ILs were instead examined. This comparison is justifiable, since both the OTf and NTf_2 anions are weakly coordinating and, where data are available, substitution of these two anions does not significantly alter the solvating parameters of the IL. The dielectric constant, the E_T value for polarity and the Kamlet–Taft parameter π^* for polarisability for the three ILs are summarised in Table 3.

Table 3. Solvent properties under ambient conditions of the triflimide ILs that yielded the de-layered morphology in MoS_2.

	Dielectric constant ε[a]	Reichardt's E_T polarity scale[b]	Kamlet–Taft dipolarity/ polarisability parameter π^*[c]
[C_1C_4IM][NTf_2]	11.6	0.64	0.955
[C_4Py][NTf_2]	11.5	0.65	0.972
[C_1C_4Pyr][NTf_2]	11.9	0.55	0.971

[a] Literature values from Krossing et al.[26] [b] Literature values from Reichardt.[27] [c] Literature values from D'Anna et al.[28]

Consistent with the findings of Wu et al., both the [C_1C_4IM] and [C_4Py] ILs have lower dielectric constants and yielded products of better crystallinity. However, these two ILs also exhibited better solvating ability compared to the [C_1C_4Pyr] IL based on the E_T polarity scale, which measures a combination of both hydrogen bonding acidity and polarisability (π^*).[29] Another noteworthy observation is that the polarisability parameter of the IL π^* appears to correlate with the catalyst activity of the de-layered MoS_2 sample, but not with the crystallinity of the product. Presently it is uncertain whether this correlation has a causal relationship. It is, however, certain that the mechanism proposed by Wu et al., regarding the supersaturation due to reduced solubility of the precursor in solvent with low dielectric constant, is not a satisfactory explanation for the present case. Since the thiomolybdate anion is a hydrogen-bond acceptor,[30] hydrogen bonding is considered to be the dominant solvating interaction for this precursor. Moreover, electrostatic models of solvation (i.e., those based on physical constants such as dielectric constant, permanent dipole moment and refractive index) often fail in rationalising solvent effects, as they do not account for specific solvent/solute interactions.[31] One postulate for the improved crystallinity is that ILs with higher hydrogen-bond acidity are better able to solubilise the precursor or crystal nuclei. This may lead to a controlled crystallisation or growth process, and thus afford products with either a reduced number of crystal defects or well-ordered edge sites. Obviously, a number of other solvent properties may also affect the outcome of the crystallisation, and these include solvent viscosity, steric hindrance and surface tension. It is expected that future investigations into the mechanism of MoS_2 crystallisation and the mode of interactions of the ILs with both the thiomolybdate precursor and the MoS_2 crystals will yield insights into methods of controlling the degree of crystallisation.

Conclusion

The ability to predictably and synthetically manipulate crystallinity and morphology of the layered crystal MoS_2 is highly desirable for catalytic applications, since the former determines the formation of well-defined active sites, and the latter affects the exposure and accessibility of substrates to these sites. This article demonstrates that control over these two properties can be exercised by judicious selection of IL as solvent for thermal decomposition of $(NH_4)_2MoS_4$ to MoS_2. It was shown that non-coordinating aromatic ILs yielded the most active MoS_2 HER electrocatalysts, which have high crystallinity and a de-layered/unstacked morphology. Based on the present results, it was postulated that intermolecular interactions exerted by the IL govern the characteristics of the MoS_2 crystals, specifically hydrogen-bond acidity for improving crystallinity, and aromatic or planar IL molecular cations for the formation of the de-layered mor-

phology. These findings provide the basis for several synthetic strategies to improve the activity of MoS_2 HER electrocatalysts, and may also have implications for preparing more active MoS_2 catalysts for the industrially important hydrodeoxygenation and hydrodesulfurisation reactions.

Experimental Section

All chemicals were of reagent grade and used without further purification. Water was purified with an Elix Millipore 100 water purification system and deoxygenated by purging with nitrogen gas overnight. The MoS_2 precursor $(NH_4)_2MoS_4$ was synthesised according to a literature procedure.[32] ^{1}H (300.13 MHz) and ^{13}C NMR (74.5 MHz) spectra were recorded on a Bruker AVANCE 300 spectrometer. Sample solutions were prepared in deuterated solvents (Cambridge Isotopes Laboratories); spectra were referenced internally to the residual solvent absorbances.[31] ESI-MS spectra were collected on a Finnigan LCQ mass spectrometer at the Mass Spectrometry Unit in the School of Chemistry, University of Sydney. Elemental analyses were performed at the Microanalytical Unit at the Research School of Chemistry, Australian National University. CHN quantifications were performed on a Carlo Erba 1106 CHN analyser; fluorine and sulfur analyses were performed on a Dionex Ion Chromatography Analyser. Thermogravimetric analyses were carried out on a TA Instruments 2950 TGA. Each sample was loaded onto a platinum pan and decomposed under a N_2 stream (10 mL min^{-1}) at 1 °C min^{-1} from ambient temperature to 500 °C.

Synthesis of 1-butyl-3-methylimidazolium trifluoromethanesulfonate: The title compound was prepared by anion exchange of 1-butyl-3-methylimidazolium bromide with sodium trifluoromethanesulfonate. The bromide salt was prepared by heating a mixture of 1-bromobutane (8.76 g, 63.9 mmol) and 1-methylimidazole (5.00 g, 60.9 mmol) under N_2 at 40 °C overnight. Unconverted substrate was removed by washing with hexane (4×50 mL), and the product was dried at 100 °C in vacuo overnight. For anion exchange, the bromide salt (5.00 g, 22.8 mmol) in acetone (50 mL) was mixed with sodium trifluoromethanesulfonate (4.12 g, 24.0 mmol) in acetone (50 mL), and NaBr immediately formed as a white precipitate. After stirring overnight, the mixture was filtered through Celite to remove the NaBr precipitate and the acetone solvent was removed at 40 °C in vacuo. The resulting oil was re-dissolved in dichloromethane (200 mL) and washed with water in 5 mL aliquots until the aqueous phase was free of bromide by testing for the formation of precipitate with $AgNO_3$ solution (0.3 M). Typically, this step involved 4–6 washings to be halide-free. The dichloromethane phase was then washed with a further 2×5 mL water to ensure minimisation of bromide impurity. The dichloromethane solvent was removed by heating at 100 °C in vacuo overnight. Yield: 80 %. ^{1}H NMR (in CD_3CN): δ=0.90 (t, 3H, $^3J_{HH}$=7.36 Hz, CH_3CH$_2$), 1.31 (sxt, 2H, $^3J_{HH}$=7.47 Hz, CH$_3$CH_2CH$_2$), 1.82 (quin, 2H, $^3J_{HH}$=7.50 Hz, CH$_2$CH_2CH$_2$), 3.87 (s, 3H, NCH$_3$), 4.17 (t, 2H, $^3J_{HH}$=7.28 Hz CH$_2$N), 7.46 (m, H, CHC*H*N), 7.51 (m, H, CHC*H*N), 8.74 ppm (s, H, NCHN); ^{13}C{^{1}H} NMR (in CD_3CN): δ=13.76 (*C*H$_3$CH$_2$), 20.02 (CH$_3$*C*H$_2$CH$_2$), 32.67 (CH$_2$*C*H$_2$CH$_2$), 36.82 (NCH$_3$), 50.29 (N*C*H$_2$CH$_2$), 122.08 (q, CF$_3$, $^1J_{CF}$=320.60 Hz), 123.41 (N*C*HCH), 124.71 (N*C*HCH), 137.46 ppm (NCHN); ^{19}F NMR (in CD_3OD): δ=−77.75 ppm (CF$_3$S); MS (ESI +ve ion): *m*/*z* (%): 138.73 (100) [C$_1$C$_4$IM]$^+$, 426.53 (37) [C$_1$C$_4$IM]$_2$[OTf]$^+$; MS (ESI −ve ion): *m*/*z* (%): 148.93 (100) [OTf]$^-$, 436.6 (16) [C$_1$C$_4$IM][OTf]$^{2-}$, 724.60 (50) [C$_1$C$_4$IM]$_2$[OTf]$^{3-}$.

Synthesis of *N*-butylpyridinium trifluoromethanesulfonate: An identical procedure to synthesising 1-butyl-3-methylimidazolium trifluoromethanesulfonate was employed, using pyridine in place of 1-methylimidazole. Yield: 81 %. M.p. 33–36 °C; T_{decomp}=365 °C; ^{1}H NMR (in D_2O): δ=0.96 (t, 3H, $^3J_{HH}$=7.34 Hz, CH_3CH$_2$), 1.38 (sxt, 2H, $^3J_{HH}$=7.50 Hz, CH$_3$CH_2CH$_2$), 2.02 (quin, 2H, $^3J_{HH}$=7.51 Hz, CH$_2$CH_2CH$_2$), 4.63 (t, 2H, $^3J_{HH}$=7.29 Hz, CH$_2$CH_2N), 8.08 (t, 1H, $^3J_{HH}$=6.82 Hz, CHC*H*CHN), 8.56 (t, 2H, $^3J_{HH}$=7.89 Hz, CHC*H*CH), 8.86 ppm (d, 2H, $^3J_{HH}$=5.88 Hz, CHC*H*N); ^{13}C{^{1}H} NMR (in D_2O): δ=13.17 (*C*H$_3$CH$_2$), 19.22 (CH$_3$*C*H$_2$CH$_2$), 33.10 (CH$_2$*C*H$_2$CH$_2$), 62.27 (NCH$_2$), 120.35 (q, $^1J_{FC}$=318.23 Hz, F$_3$*C*S), 128.81 (CH*C*HCH), 144.69 (t, $^1J_{CN}$=8.01 Hz, CH*C*HN), 146.09 ppm (NCH*C*HCH); ^{19}F NMR (in CD_3OD): δ=−77.55 ppm (CF$_3$S); MS (ESI +ve ion): *m*/*z* (%): 136 (100) [C$_4$Py]$^+$, 421 (45) [C$_4$Py]$_2$[OTf]$^+$; MS (ESI −ve ion): *m*/*z* (%): 149 (100) [OTf]$^-$, 434 (33) [C$_4$Pyr][OTf]$^{2-}$, 719 (30) [C$_4$Pyr]2[OTf]$^{3-}$; elemental analysis (%) found (calcd): C 42.44 (41.10), H 4.80 (4.95), N 5.05 (4.91), F 19.95 (19.98), S 11.46 (11.24).

Synthesis of *N*-butylpyridazinium trifluoromethanesulfonate: An identical procedure to synthesising 1-butyl-3-methylimidazolium trifluoromethanesulfonate was employed, using pyridazine in place of 1-methylimidazole. Yield: 76 %. T_{decomp}=319 °C; ^{1}H NMR (in D_2O): δ=0.98 (t, 3H, $^3J_{HH}$=7.39 Hz, CH_3CH$_2$), 1.42 (sxt, 2H, $^3J_{HH}$=7.92 Hz, CH$_3$CH_2CH$_2$), 2.12 (quin, 2H, $^3J_{HH}$=7.72 Hz, CH$_2$CH_2CH$_2$), 4.90 (t, 2H, $^3J_{HH}$=7.52 Hz, NCH_2CH$_2$), 8.54 (m, 1H, CHC*H*NNCH$_2$), 8.62 (m, 1H, CHC*H*NCH$_2$), 9.53 (d, 1H, $^3J_{HH}$=3.95 Hz, NC*H*CH), 9.74 ppm (d, 1H, $^3J_{HH}$=5.77 Hz, C*H*NCH$_2$); ^{13}C{^{1}H} NMR (in $CDCl_3$): δ=13.30 (*C*H$_3$CH$_2$), 19.30 (CH$_3$*C*H$_2$CH$_2$), 32.16 (CH$_2$*C*H$_2$CH$_2$), 65.94 (N*C*H$_2$CH$_2$), 120.56 (q, CF$_3$, $^1J_{CF}$=320.47 Hz), 136.56 (NNCH*C*H), 136.73 (NCH*C*H), 150.25 (CH$_2$N*C*H), 154.13 ppm (CH$_2$NN*C*H); MS (ESI +ve ion): *m*/*z* (%): 136.67 (100) [C$_4$Pyz]$^+$, 422.47 (20) [C$_4$Pyz]$_2$[OTf]$^+$, 708.40 (13) [C$_4$Pyz]$_3$[OTf]$^{2+}$; MS (ESI −ve ion): *m*/*z* (%): 148.87 (100) [OTf]$^-$, 434.47 (7) [C$_4$Pyz][OTf]$^{2-}$; elemental analysis (%) found (calcd): C 37.61 (37.76), H 4.88 (4.58), N 9.48 (9.79), F 19.64 (19.91), S 10.69 (11.20).

Synthesis of *N*-butyl-*N*-methylpyrrolidinium trifluoromethanesulfonate: An identical procedure to synthesising 1-butyl-3-methylimidazolium trifluoromethanesulfonate was employed, using *N*-methylpyrrolidine in place of 1-methylimidazole. Yield: 87 %. T_{decomp}=356 °C; ^{1}H NMR (in D_2O): δ=0.95 (t, 3H, $^3J_{HH}$=7.37 Hz, CH_3CH$_2$), 1.38 (sxt, 2H, $^3J_{HH}$=7.42 Hz, CH$_3$CH_2CH$_2$), 1.71 (m, 2H, CH$_2$CH_2CH$_2$), 2.21 (m, 4H, Pyr, CH_2CH$_2$N), 3.04 (s, 3H, CH_3N), 3.34 (m, 2H, CH$_2$CH_2N), 3.53 ppm (m, 4H, Pyr, CH$_2$CH_2N); ^{13}C{^{1}H} NMR (in CD_3CN): δ=13.20 (*C*H$_3$CH$_2$), 19.77 (CH$_3$*C*H$_2$CH$_2$), 21.71 (Pyr, NCH$_2$*C*H$_2$), 25.63 (CH$_2$*C*H$_2$CH$_2$), 48.52 (t, $^1J_{CN}$=4.06 Hz, NCH$_3$), 64.32 (t, $^1J_{CN}$=2.79 Hz, N*C*H$_2$CH$_2$), 64.61 (t, $^1J_{CN}$=2.95 Hz, pyr, N*C*H$_2$CH$_2$), 121.48 ppm (q, $^1J_{CF}$=320.89 Hz, CF$_3$); ^{19}F NMR (in CD_3OD): δ=−77.64 ppm (CF$_3$S); MS (ESI +ve ion): *m*/*z* (%): 142.2 (100) [C$_1$C$_4$Pyr]$^+$, 432.87 (19) [C$_1$C$_4$Pyr]$_2$[OTf]$^+$; MS (ESI −ve ion): *m*/*z* (%): 149.33 (100) [OTf]$^-$, 440.00 (66) [C$_1$C$_4$Pyr][OTf]$^{2-}$; elemental analysis (%) found (calcd): C 40.85 (41.23), H 7.26 (6.92), N 4.79 (4.81), F 16.04 (19.56), S 9.80 (11.00).

Synthesis of *N*-butyl-*N*-methylpiperidinium trifluoromethanesulfonate: An identical procedure to synthesising 1-butyl-3-methylimidazolium trifluoromethanesulfonate was employed, using *N*-methylpiperidine in place of 1-methylimidazole. Yield: 67 %. T_{decomp}=350 °C; ^{1}H NMR (in $CDCl_3$): δ=0.99 (t, 3H, $^3J_{HH}$=6.75 Hz, CH_3CH$_2$), 1.42 (sxt, 2H, $^3J_{HH}$=8.19 Hz, CH$_3$CH_2CH$_2$), 1.82–1.96 (m, 2H, PI, NCH$_2$ CH$_2$CH_2; m, 6H, NCH$_2$CH_2), 3.10 (s, 3H, NCH$_3$), 3.32–3.48 ppm (m, 6H, CH$_2$N); ^{13}C{^{1}H} NMR (in $CDCl_3$): δ=13.36 (*C*H$_3$CH$_2$), 19.44 (CH$_3$*C*H$_2$CH$_2$), 19.86 (PI, NCH$_2$*C*H$_2$), 20.52 (PI, NCH$_2$CH$_2$*C*H$_2$), 23.53 (NCH$_2$*C*H$_2$), 47.35 (NCH$_3$), 60.88 (PI, NCH$_2$), 63.65 (NCH$_2$), 120.65 ppm (q, CF$_3$, $^1J_{CF}$=319.87 Hz); MS (ESI +ve ion): *m*/*z* (%): 156 (100) [C$_1$C$_4$PI]$^+$, 461 (31, [C$_1$C$_4$PI]$_2$[OTf]$^+$); MS (ESI −ve ion): *m*/*z* (%): 149 (100) [OTf]$^-$, 454 (27) [C$_1$C$_4$PI][OTf]$^{2-}$; elemental analysis (%) found (calcd): C 43.50 (43.27), H 7.52 (7.26), N 4.77 (4.59), F 18.76 (18.67), S 10.47 (10.50).

Synthesis of *N*-butyl-*N*-methylmorpholinium trifluoromethanesulfonate: An identical procedure to synthesising 1-butyl-3-methylimidazolium trifluoromethanesulfonate was employed, using *N*-methylmorpholine in place of 1-methylimidazole. The purification step of the anion exchange was modified, since the protocol involving the washing of the dichloromethane phase with water resulted in unacceptable yield. Instead, residual bromide was removed by passing the dichloromethane solution through an activated neutral alumina column. The eluent was found to be bromide-free by the absence of precipitate when mixed with an aqueous solution of $AgNO_3$ (0.3 M). Yield: 49 %. T_{decomp}=349 °C; ^{1}H NMR (in [D$_6$]acetone): δ=1.00 (t, 3H, $^3J_{HH}$=7.37 Hz, CH_3CH$_2$), 1.46 (sxt, 2H, $^3J_{HH}$=7.32 Hz, CH$_3$CH_2CH$_2$), 1.90 (m, 2H, CH$_2$CH_2CH$_2$), 3.39 (m, 3H, NCH$_3$), 3.67 (m, 4H, NCH$_2$, MO; m, 2H, NCH$_2$, Bu), 4.09 ppm (m, 4H, OCH_2); ^{13}C{^{1}H} NMR (in [D$_6$]acetone): δ=13.88 (*C*H$_3$CH$_2$), 20.18 (CH$_3$*C*H$_2$CH$_2$), 23.48 (NCH$_2$*C*H$_2$), 47.01 (NCH$_3$), 47.28 (N*C*H$_2$CH$_2$),

60.54 (MO, NCH_2), 61.21 (MO, OCH_2), 122.05 ppm (q, CF_3, $^1J_{CF}$= 321.87 Hz); MS (ESI +ve ion): *m/z* (%): 158 (100) $[C_1C_4MO]^+$, 465 (33) $[C_1C_4MO]_2[OTf]^+$; MS (ESI −ve ion): *m/z* (%): 149 (100) $[OTf]^-$, 456 (36) $[C_1C_4MO][OTf]^{2-}$; elemental analysis (%) found (calcd): C 37.17 (36.92), H 6.70 (6.82), N 4.34 (4.31), F 17.45 (17.52), S 9.85 (9.85).

Synthesis and characterisation of MoS_2: The ionic liquid (3.00 g) was dried overnight at 100 °C in vacuo before use. $(NH_4)_2MoS_4$ (150 mg) was dissolved in the ionic liquid at 40 °C to form a deep red solution. This solution was then heated at 300 °C under a H_2/N_2 flow (10 %, 10 mL min^{-1}) for 2 h, yielding a black suspension. Ethanol was added to this suspension and the black MoS_2 powder and the ionic liquid were separated by centrifugation. The MoS_2 was further washed with ethanol (5×50 mL), followed by water (2×15 mL), acetone (2×15 mL) and finally hexane (2× 15 mL). The solid was then dried in vacuo at ambient temperature. Up to 80 % of the ionic liquid can be recovered by removing the ethanol in vacuo.

Transmission electron microscopy was performed on a Philips CM120 Biofilter microscope operating at 120 kV. Images were digitally recorded on a Gatan slow-scan CCD camera. Each sample was prepared by dispersing the sample powder in ethanol and drop-casting onto a 200 mesh copper grid coated with holey carbon (ProSciTech). XRD patterns were recorded with a PANalytical X′Pert PRO MPD X-ray diffractometer set up in Bragg PDS mode with a PIXcel detector and $Cu_{K\alpha}$ (λ=1.5419 Å) as irradiation source. The samples were loaded on zero-background silicon wafers on a spinning sample holder. Scans were carried out from 10 to 80° in 2θ with step size of 0.013° in 2θ at a scan rate of 0.0525° s^{-1}. FTIR spectra of the MoS_2 samples were collected as NaBr matrices on a Varian Scimitar 800 FTIR spectrometer with NaBr as spectroscopic background. Raman spectra of the MoS_2 samples were collected on a Renishaw Raman Invia Reflex spectrometer. The samples were excited with a 514 nm argon laser at 10× objective and 10 s exposure for one scan in the range of 100–3000 cm^{-1}. Surface areas of the samples were measured by nitrogen sorption analysis on a Micromeritics Accelerated Surface Area & Porosimetry System (ASAP) 2020 instrument. The powder sample was weighed out (50–70 mg) and outgassed at 90 °C at 7 μbar for at least 4 h. Nitrogen adsorption and desorption isotherms were collected at 77 K, and the surface areas were calculated by using the BET model in the framework of the Micromeritics software. The BET surface area of MoS_2-$[C_1C_4IM][OTf]$ is significantly higher than that reported previously.[7] This difference is attributed to the more rigorous purification steps adopted in this work. As stated above, the MoS_2 powder was washed with, in addition to ethanol, water, acetone and hexane, which ensures complete removal of trace IL and starting materials.

Electrochemical determination of HER activity: Hydrodynamic electrochemical experiments were performed on a BAS 100B Electrochemical Workstation, connected to a BAS RDE-1 set-up. The working rotating electrode was a 3 mm glassy carbon electrode (BAS), polished with alumina (1 μm) on a Buehler pad according to BAS guidelines before use. A platinum wire was used as the counter-electrode; the reference electrode was an Ag|AgCl electrode (3 M NaCl, BAS). The reference electrode was calibrated with ferri- and ferrocyanide; the potential for this couple was taken as 436 mV versus the standard hydrogen electrode (SHE) at pH 7. All potentials henceforth are quoted against SHE. Modification of the working electrode was carried out as follows. The MoS_2 powder (10.0 mg) was weighed out on a Mettler Toledo XS105 balance, and then dispersed with sonication in water (10.00 mL) to achieve a dispersion concentration of 1.00 mg mL^{-1}. A 10 μL aliquot corresponding to 10 μg was drop-cast onto the glassy carbon electrode and dried under a stream of nitrogen.

HER was performed in linear-scan voltammetry mode from 562 to −637 mV at 5 mV s^{-1} scan rate and 100 μA V^{-1} sensitivity. The electrolyte was aqueous H_2SO_4 (60 mL, 0.500 M). The rotation rate was varied from 400 to 6000 rpm and the current at −533 mV was used for the Levich–Koutecky plot. The limiting current was determined by fitting the data points to a linear correlation and extrapolating the current to $\omega^{-0.5}\rightarrow 0$. For evaluation of catalyst stability and turnover frequency, HER was performed in single-potential, time-based mode. The electrode was rotated at 1000 rpm and held at −533 mV for 1 h. Hydrogen production and turnover frequency were estimated by integrating the time–current plot in the region where the current is steady, assuming a Faradaic efficiency of 100 % and that all 10 μg participated in the electrocatalytic reaction. All experiments were repeated to verify the reproducibility of the catalyst drop-casting process and the electrocatalytic activities.

Acknowledgements

We thank the Australian Centre for Microscopy & Microanalysis for use of their electron microscopes. Financial support from the University of Sydney and the Australian Research Council is gratefully acknowledged.

[1] D. A. J. Rand, R. M. Dell, *Hydrogen Energy: Challenges and Prospects*, RSC Publishing, Cambridge, **2007**.
[2] B. E. Conway, G. Jerkiewicz, *Electrochim. Acta* **2000**, *45*, 4075–4083.
[3] D. J. Evans, C. J. Pickett, *Chem. Soc. Rev.* **2003**, *32*, 268–275.
[4] S. C. Lee, R. H. Holm, *Proc. Natl. Acad. Sci. USA* **2003**, *100*, 3595–3600.
[5] B. Hinnemann, P. G. Moses, J. Bonde, K. P. Jørgensen, J. H. Nielsen, S. Horch, I. Chorkendorff, J. K. Nørskov, *J. Am. Chem. Soc.* **2005**, *127*, 5308–5309.
[6] a) J. Bonde, P. G. Moses, T. F. Jaramillo, J. K. Nørskov, I. Chorkendorff, *Faraday Discuss.* **2009**, *140*, 219–231; b) T. F. Jaramillo, K. P. Jørgensen, J. Bonde, J. H. Nielsen, S. Horch, I. Chorkendorff, *Science* **2007**, *317*, 100–102.
[7] V. W.-h. Lau, A. F. Masters, A. M. Bond, T. Maschmeyer, *ChemCatChem* **2011**, *3*, 1739–1742.
[8] B. H. Davis, *Handbook of Heterogeneous Catalysis*, Wiley-VCH, Weinheim, **2008**.
[9] a) Z. Jiang, Q. Kuang, Z. Xie, L. Zheng, *Adv. Funct. Mater.* **2010**, *20*, 3634–3645; b) Z. Ma, J. Yu, S. Dai, *Adv. Mater.* **2010**, *22*, 261–285; c) T. Xu, X. Zhou, Z. Jiang, Q. Kuang, Z. Xie, L. Zheng, *Cryst. Growth Des.* **2009**, *9*, 192–196; d) X. Zhou, Z. Xie, Z. Jiang, Q. Kuang, S. Zhang, T. Xu, R. Huang, L. Zheng, *Chem. Commun.* **2005**, 5572–5574.
[10] a) M. Daage, R. R. Chianelli, *J. Catal.* **1994**, *149*, 414–427; b) H. Farag, K. Sakanishi, M. Kouzu, A. Matsumura, Y. Sugimoto, I. Saito, *J. Mol. Catal. A* **2003**, *206*, 399–408; c) C. T. Tye, K. J. Smith, *Catal. Today* **2006**, *116*, 461–468.
[11] Y. Iwata, Y. Araki, K. Honna, Y. Miki, K. Sato, H. Shimada, *Catal. Today* **2001**, *65*, 335–341.
[12] a) U. Zimmermann, N. Karl, *Surf. Sci.* **1992**, *268*, 296–306; b) T. Fukushima, A. Kosaka, Y. Ishimura, T. Yamamoto, T. Takigawa, N. Ishii, T. Aida, *Science* **2003**, *300*, 2072–2074; c) T. Fukushima, T. Aida, *Chem. Eur. J.* **2007**, *13*, 5048–5058; d) N. Liu, F. Luo, H. Wu, Y. Liu, C. Zhang, J. Chen, *Adv. Funct. Mater.* **2008**, *18*, 1518–1525; e) P. G. Moses, J. J. Mortensen, B. I. Lundqvist, J. K. Nørskov, *J. Chem. Phys.* **2009**, *130*, 104709.
[13] F. Maugé, J. Lamotte, N. S. Nesterenko, O. Manoilova, A. A. Tsyganenko, *Catal. Today* **2001**, *70*, 271–284.
[14] A. A. Tsyganenko, F. Can, A. Travert, F. Maugé, *Appl. Catal. A* **2004**, *268*, 189–197.
[15] D. Liu, W. W. Lei, J. Hao, D. D. Liu, B. B. Liu, X. Wang, X. H. Chen, Q. L. Cui, G. T. Zou, J. Liu, S. Jiang, *J. Appl. Phys.* **2009**, *105*, 023513.
[16] G. L. Frey, R. Tenne, M. L. Matthews, M. S. Dresselhaus, G. Dresselhaus, *Phys. Rev. B* **1999**, *60*, 2883–2892.
[17] D. Yang, S. Jiménez Sandoval, W. M. R. Divigalpitiya, J. C. Irwin, R. F. Frindt, *Phys. Rev. B* **1991**, *43*, 12053–12056.
[18] J. H. Nielsen, L. Bech, K. Nielsen, Y. Tison, K. P. Jørgensen, J. L. Bonde, S. Horch, T. F. Jaramillo, I. Chorkendorff, *Surf. Sci.* **2009**, *603*, 1182–1189.
[19] E. Matijević, *Chem. Mater.* **1993**, *5*, 412–426.
[20] a) D. Matoga, J. Szklarzewicz, J. Fawcett, *Polyhedron* **2005**, *24*, 1533–1539; b) S. Gupta, S. Pal, A. K. Barik, S. Roy, A. Hazra, T. N.

Mandal, R. J. Butcher, S. K. Kar, *Polyhedron* **2009**, *28*, 711–720; c) S. Gupta, S. Roy, T. N. Mandal, K. Das, S. Ray, R. J. Butcher, S. K. Kar, *J. Chem. Sci.* **2010**, *122*, 239–245; d) D. Matoga, J. Szklarzewicz, K. Lewiński, *Polyhedron* **2010**, *29*, 94–99.

[21] a) S. Fletcher, *J. Solid State Electrochem.* **2009**, *13*, 537–549; b) A. J. Appleby, J. H. Zagal, *J. Solid State Electrochem.* **2011**, *15*, 1811–1832.

[22] Z. Chen, D. Cummins, B. N. Reinecke, E. Clark, M. K. Sunkara, T. F. Jaramillo, *Nano Lett.* **2011**, *11*, 4168–4175.

[23] M. Pourbaix, *Atlas of electrochemical equilibria in aqueous solutions*, 2nd ed., NACE International, Houston, Texas, **1974**.

[24] J. Wu, X. Lu, L. Zhang, F. Huang, F. Xu, *Eur. J. Inorg. Chem.* **2009**, 2789–2795.

[25] V. W.-h. Lau, L. G. A. van de Water, A. F. Masters, T. Maschmeyer, *Chem. Eur. J.* **2012**, *18*, 2923–2930.

[26] I. Krossing, J. M. Slattery, C. Daguenet, P. J. Dyson, A. Oleinikova, H. Weingärtner, *J. Am. Chem. Soc.* **2006**, *128*, 13427–13434.

[27] C. Reichardt, *Green Chem.* **2005**, *7*, 339–351.

[28] F. D'Anna, S. La Marca, P. Lo Meo, R. Noto, *Chem. Eur. J.* **2009**, *15*, 7896–7902.

[29] Y. Marcus, *Chem. Soc. Rev.* **1993**, *22*, 409–416.

[30] B. R. Srinivasan, S. N. Dhuri, M. Poisot, C. Näther, W. Bensch, *Z. Naturforsch. B: Chem. Sci.* **2004**, *59*, 1083–1092.

[31] C. Reichardt, *Chem. Rev.* **1994**, *94*, 2319–2358.

[32] R. S. Reid, R. J. Clark, E. K. Quagraine, *Can. J. Chem.* **2007**, *85*, 1083–1089.

[33] H. E. Gottlieb, V. Kotlyar, A. Nudelman, *J. Org. Chem.* **1997**, *62*, 7512–7515.

Received: January 24, 2012
Revised: March 18, 2012
Published online: May 15, 2012

